

Influence of jet depth on the equatorial jet direction on giant planets

Yaoxuan Zeng^{a,1}, Wanying Kang^b, Glenn R. Flierl^b, and Geoffrey K. Vallis^c

Submitted to Proceedings of the National Academy of Sciences for consideration

It remains puzzling why, despite their similar nature, Jupiter and Saturn possess a prograde equatorial jet, whereas Uranus and Neptune have a retrograde one. To understand this discrepancy, we use a 2-D quasi-geostrophic model to explore how the penetration depth of the jet, regulated by Ohmic dissipation, influences jet patterns. When jets penetrate deeply into the planet's interior, the Taylor column height decreases equatorward in the equatorial jet region, yielding a negative gradient of planetary potential vorticity (i.e., a negative β effect). The tendency to eliminate such a gradient leads to a prograde equatorial jet, as observed on Jupiter and Saturn. In contrast, a relatively shallow system favors retrograde jets along the equator due to the positive β effect of geometry. If the proposed mechanism applies to Uranus and Neptune, the observed jet structure may suggest the presence of a stratified layer or Ohmic dissipation layer near their surfaces.

Giant planets | Jet formation | Quasi-geostrophic | PV mixing

Zonal jets are expected to form on fast-rotating giant planets, and their existence on Jupiter, Saturn, Uranus and Neptune has been captured by various missions during flybys (1–8). It is revealed that the jet profiles of these planets fall into two distinct categories. Jupiter and Saturn exhibit multiple jets in each hemisphere, with particularly strong prograde jets near the equator (hereafter, JS-type jet, Fig. 1a). In contrast, Uranus and Neptune have only one jet in each hemisphere, and their equatorial jets are retrograde (hereafter, UN-type jet, Fig. 1b). The differences in the four giant planets' jet characteristics clearly pose an intriguing puzzle about jet formation mechanisms, and addressing this puzzle may offer us an opportunity to infer the interior properties of these planets.

Two jet formation mechanisms have been proposed in the attempts to address this puzzle. The first considers a deep atmosphere energized by convection due to bottom heating (9–20), whereas the second considers a shallow atmosphere powered by baroclinic instability induced by the poleward cooling trend and convection due to intrinsic heating (21–27). Both frameworks are able to reproduce some features of the JS-type and UN-type jets in 3-D numerical simulations. However, they are studied under two distinct model configurations, and they have no consensus on how the direction of the equatorial jet depends on intrinsic heat flux. In the deep atmosphere framework (15), a prograde equatorial jet forms under weak convective forcing, as the tilted convective mode near the equator (thermal Rossby waves, or Busse mode (10)) transports prograde momentum toward the surface. Under stronger convective forcing, the equatorial jet reverses direction as turbulence disrupts the tilted structure of the convective rolls and mixes low-angular momentum air from the deep interior to the surface. In contrast, in the shallow atmosphere framework (25, 26), a retrograde jet forms near the equator when intrinsic heating is weak, because air transported from high latitudes to equator has lower angular momentum and accelerates in the retrograde direction when mixed equatorward. With strong intrinsic heating, prograde jet forms near the equator, as the convection-driven equatorial Rossby waves will converge prograde momentum towards the equator.

The deep and shallow frameworks are very different in their domain geometries, their governing equations, and their energy sources, making it challenging to make direct comparisons. Attempts to build a 3-D model that resolves both deep convection and baroclinic eddies proves to be computationally infeasible given the two processes' drastically different spatial scale (28). Here, we intend to use a 2-D model to bridge the gap between the deep and shallow frameworks. It is possible to reduce one dimension, because on fast-rotating planets, motions are largely invariant along the rotation axis, following the Taylor-Proudman Theorem (29). The four giant planets are all in this fast-rotating regime characterized by Rossby numbers

Significance Statement

Zonal jets are the most prominent feature of atmosphere circulation on the four giant planets in the solar system. Despite having similar energy sources, intrinsic heating and solar radiation, the four planets have distinct jet structures: Jupiter and Saturn have prograde equatorial jets, while Uranus and Neptune have retrograde ones. What determines the direction of the equatorial jet remains an open question. We find that the jet penetration depth is a primary control factor of the equatorial jet direction. Specifically, deep atmospheres favor prograde equatorial jets, while shallow atmospheres favor retrograde equatorial jets. This finding provides a way to infer planetary interiors solely from surface wind observations, which can be tested through future gravity field measurements of these planets.

Author affiliations: ^aDepartment of the Geophysical Sciences, The University of Chicago, Chicago, 60637, USA.; ^bEarth, Atmospheric and Planetary Science Department, Massachusetts Institute of Technology, Cambridge, 02139, USA.; ^cMathematics and Statistics, University of Exeter, Exeter, UK

Y.Z., W.K., G.F., and G.V. designed research. Y.Z. performed research, contributed new analytic tools, and analyzed data. Y.Z. and W.K. wrote the paper.

The authors declare that they have no competing interests.

¹To whom correspondence should be addressed. E-mail: yxzeng@uchicago.edu

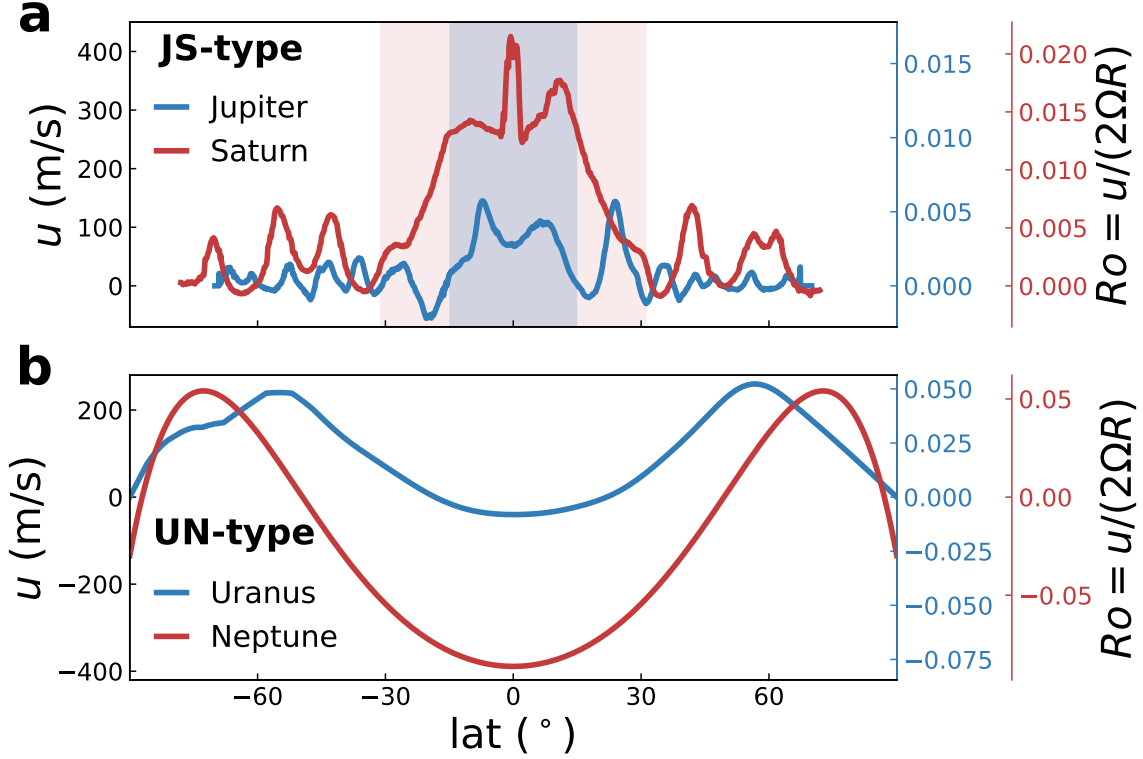


Fig. 1. Observed surface zonal wind profile on giant planets. The JS-type jets are shown in **a** and the UN-type jets are shown in **b**. The shading regions in **a** indicate regions outside the tangent cylinder, with blue representing Jupiter and red representing Saturn. For Uranus and Neptune, the tangent cylinder latitude is less well constrained. The Rossby number of the flow, $Ro = U/(2\Omega R)$ where U is the velocity, Ω is the rotation rate, and R is the planetary radius, is also shown. For Jupiter, data were obtained from Juno’s third perijove pass on December 11, 2016 (7). For Saturn, measurements were taken from Cassini ISS MT2 and MT3 images spanning 2004 to 2009 (5). For Uranus and Neptune, due to limited observations, fitted curves are used, based on (6) and (2), respectively.

much smaller than unity (26) (Fig. 1). This model means to capture how small-scale eddies, after being generated, organize themselves into coherent structures such as zonal jets (30, 31). As elaborated below, instead of trying to resolve the eddy generation process, the expected vorticity anomalies are directly injected into the model as stochastic noise without distinguishing the two forcing mechanisms (convection v.s. baroclinic instability). Also, our model provides the flexibility to prescribe the effects of the domain depth as needed. These two features allow us to contrast the deep and shallow scenarios within the same framework. Furthermore, the 2-D framework enables us to explore a wider parameter space with limited computational resources.

The governing equation of our model is obtained by integrating the vorticity equation in the rotational axis (see *Supporting Information*):

$$\frac{Dq}{Dt} = \mathcal{F}(\varepsilon) - \mu\zeta - \nu_h \nabla^4 \zeta, \quad q = \zeta - \frac{\psi}{L_d^2} + \int_0^y \beta dy', \quad [1]$$

where q is the potential vorticity (PV), ψ is the stream function satisfying $u = -\partial\psi/\partial y$ and $v = \partial\psi/\partial x$, $\zeta \equiv \partial v/\partial x - \partial u/\partial y$ is the vorticity, and u and v are velocities along x and y , respectively. Ω is the planetary rotation rate, and $\beta = (-2\Omega/H)(dH/dy)$ is the planetary Potential Vorticity (PV) gradient due to the spherical geometry, determined by H , the column depth parallel to rotation axis (Fig. 2). L_d

is the Rossby deformation radius, representing the effect of stratification in the atmosphere (32, 33). \mathcal{F} is the stochastic eddy source term used to parameterize the energy injection by convection or baroclinic eddies, whose magnitude depends on the energy injection rate ε . μ is the linear damping coefficient representing jet dissipation by the planet’s electromagnetic field at the bottom of the domain (Ohmic dissipation) (34–36). The strong linear damping is only present inside the tangent cylinder where the atmospheric column is in direct contact with the Ohmic dissipation layer. ν_h is the hyperviscosity coefficient to ensure numerical stability (a detailed description of the model configuration can be found in *Supporting Information*). We carry out numerical simulations with four different energy injection rates ($\varepsilon = 5 \times 10^{-10}$, 2.9×10^{-11} , 1.7×10^{-12} , and 10^{-13}) along with two different linear damping coefficients ($\mu = 5 \times 10^{-8}$ and 10^{-7}), applying two different β profiles to each simulation, representing the deep versus shallow scenario (Fig. 2b & d). Two different deformation radii are considered, one with $L_d \rightarrow \infty$ representing a bounded unstratified atmosphere, the other with a finite L_d representing the internal mode in a stratified atmosphere. Using this model, we will demonstrate how the direction of the equatorial jet, the width and number of jets are governed by the jet penetration depth and the energy injected into the jets.

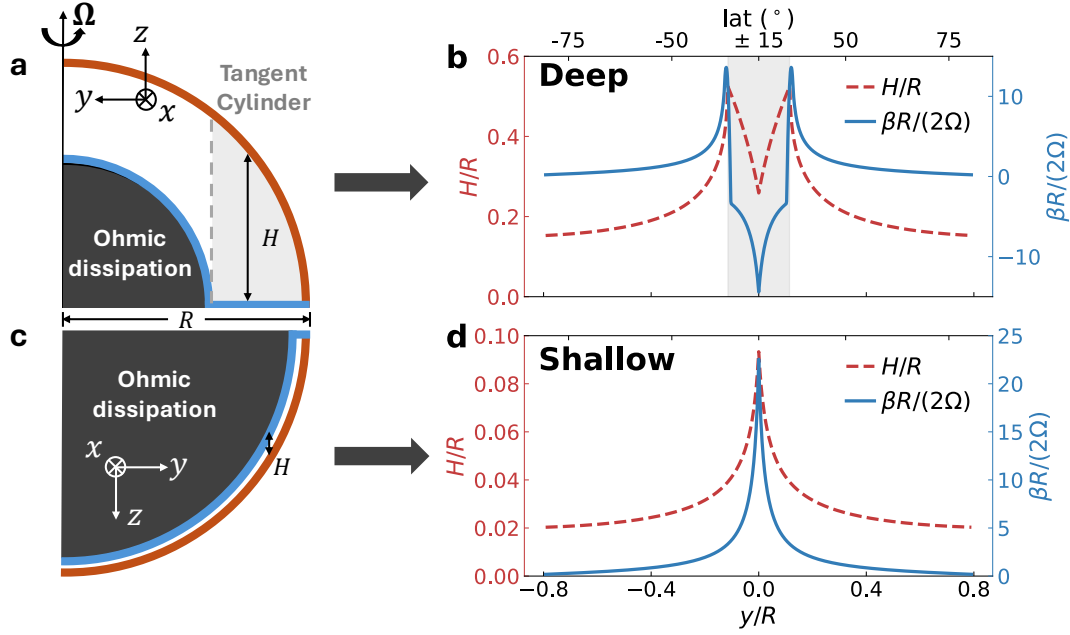


Fig. 2. Geometry of the atmosphere on giant planets and the corresponding β profile. The upper row shows the deep scenario ($D = 0.15R$, **a** and **b**), and the lower row shows the shallow scenario ($D = 0.02R$, **c** and **d**), where D is the jet penetration depth and R is the planetary radius. In the schematics (**a** and **c**), the black shaded region indicates areas where jets are damped by Ohmic dissipation. The column depth H is defined as the distance from the surface (brown line) to the bottom, marked by the Ohmic dissipation level inside the tangent cylinder and a virtual equatorial plane outside the tangent cylinder (blue line). The gray dashed line indicates the tangent cylinder, where the cylindrical air column contacts the Ohmic dissipation layer. The light gray shading indicates regions outside the tangent cylinder. All values in **b** and **d** are non-dimensionalized using planetary radius and rotation (see *Supporting Information* for detailed derivation).

Table 1. Length scales of the four giant planets in the solar system.

Property	Jupiter	Saturn	Uranus	Neptune
R (10^3 km)	71	60	26	25
Jet depth D (10^3 km)	2.38 ± 0.14	8.74 ± 0.10	< 1.10	< 1.10
L_e (km)	20.6 ± 0.2	18.2 ± 0.7	$> 8.6 \pm 2.6$	$> 13.4 \pm 0.7$
L_β (10^3 km)	1.071 ± 0.010	0.519 ± 0.017	$> 0.392 \pm 0.094$	$> 0.547 \pm 0.023$
L_{Rh} (10^3 km)	7.32	9.87	16.7	12.1
$L_{Rh,eq}$ (10^3 km)	5.25	10.0	8.46	6.11

Results

Direction of the equatorial jets. In a 2-D fluid system, small-scale eddies tend to organize themselves into larger coherent structures through a process known as the inverse energy cascade. Under the modulation of the planetary PV gradient (β), after energy cascades to a specific scale L_β , the eddies transfer their energy into zonal jets. Beyond that, energy continues cascading to larger scales until it reaches the frictional Rhines scale L_{Rh} , where it is dissipated (31). If there is a sufficiently large scale separation among the scale of the injected eddies L_e , the β scale L_β , the frictional Rhines scale L_{Rh} , and the domain scale L_{domain} , as required by $n_e \gtrsim 4n_\beta \gtrsim 8n_{Rh} \gtrsim 30n_{domain}$, the flow enters the zonostrophic regime where multiple zonal jets can form. Here, n indicates the corresponding wavenumbers, where $n_\beta = \varepsilon^{-1/5} \beta^{3/5} / 2$ and $n_{Rh} = \varepsilon^{-1/4} \beta^{1/2} \mu^{1/4} / \sqrt{2}$, following (37).

During this process, turbulent eddies mix conserved tracers within the fluid, including PV. The planetary PV gradient is counteracted by the PV gradient induced by the flow, giving rise to hyperbolic-shaped zonal jets, $\bar{u} \sim \beta(y - y_c)^2 / 2$, where

the overline denotes the zonal average and y_c is jet center (this jet shape is derived for $1/L_d = 0$ with a constant β in (29), but the argument remains valid for $1/L_d \neq 0$, as elaborated later). The kinetic energy of the system, therefore, increases with the mixing scale, so there may not be sufficient energy to homogenize PV uniformly throughout the entire domain. Consequently, PV is homogenized regionally, forming PV staircases (29). The width of these jets is constrained by the Rhines scale (L_{Rh}), which increases with the jet speed (30).

The equatorial jet profile can be obtained by solving $q = \text{const}$ at the equator, assuming a single jet outside the tangent cylinder that is symmetric about the equator. Additionally, we assume that the zonal jet speed vanishes at the tangent cylinder ($y = \pm D$, where D is the penetration depth of the jet) under the influence of damping with the Ohmic dissipation layer. The resulting equatorial jet profile is:

$$\bar{u} = \beta L_d^2 \left[\frac{\cosh(y/L_d)}{\cosh(D/L_d)} - 1 \right] \stackrel{L_d \rightarrow \infty}{\approx} \frac{\beta}{2} (y^2 - D^2). \quad [2]$$

Since the bracketed term at $y = 0$ is always negative, it can be seen that the sign of β controls the direction of the equatorial

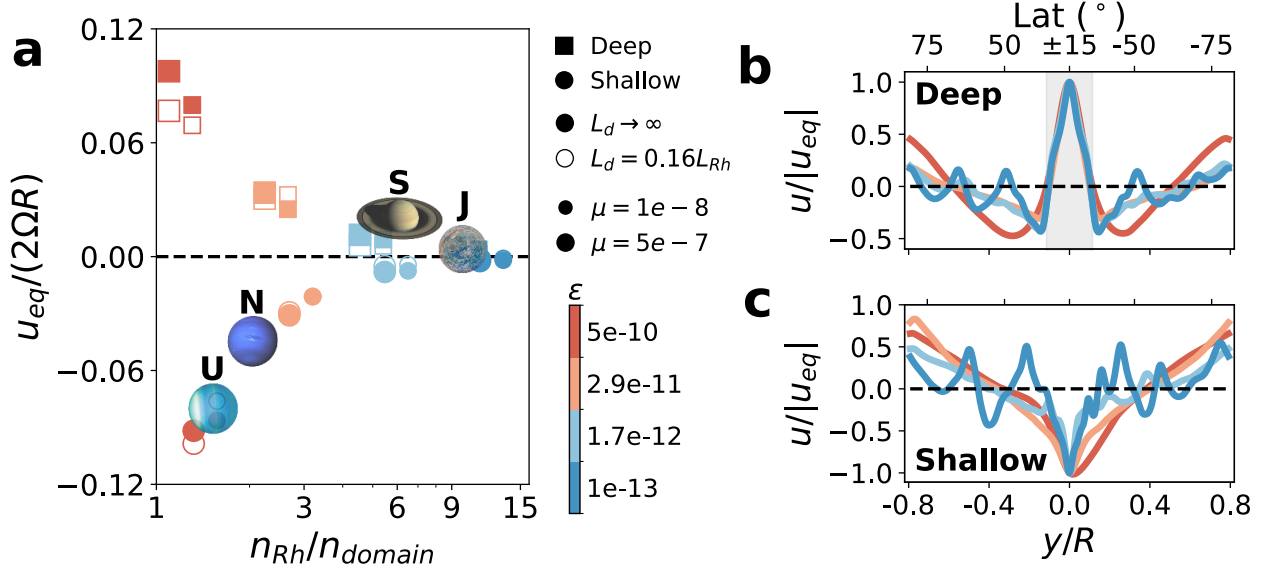


Fig. 3. The direction of the equatorial jet. **a**, Non-dimensionalized equatorial zonal jet speed ($u_{eq}/(2\Omega R)$) as a function of the ratio of the Rhines wavenumber n_{Rh} to the domain wavenumber $n_{domain} = \pi/L_{domain}$. **b** and **c**, Zonal-mean zonal velocity profiles, normalized by the equatorial jet speed magnitude ($u/|u_{eq}|$), with a deep (**b**) or shallow (**c**) β profile. Parameters for Jupiter (J), Saturn (S), Uranus (U), and Neptune (N) are also marked, with planetary parameters (38–41) shown in Table 1 (detailed calculations are discussed in Supporting Information). In **b**, the gray shading indicates regions outside the tangent cylinder in the deep cases, where $\beta < 0$. In **b** and **c**, only $\mu = 10^{-8}$ simulations are shown, with all profiles provided in Fig. S1. The line colors corresponds to marker colors in **a**, representing different energy injection rates. Planet photo credits: NASA/JPL-Caltech/SwRI/MSSS/STScI.

jet: a shallow case ($\beta > 0$ at the equator) should always lead to a retrograde equatorial jet, whereas a deep case ($\beta < 0$ at the equator) results in a prograde equatorial jet.

The jet profile in Equation 2 is obtained with a constant β . When β is not constant, it is helpful to consider the averaged β over the latitudinal range where PV homogenization occurs. Thus, the direction of the equatorial jet is likely related to whether the jet width L_{Rh} is large compared to the region with negative β , or equivalently, the penetration depth of the jet D . In the deep scenario, where $D \gtrsim L_{Rh}$, the averaged β is more likely negative, favoring a prograde jet at the equator. Conversely, in the shallow scenario, where $D \ll L_{Rh}$, the averaged β is more likely positive, favoring a retrograde jet at the equator.

The results from numerical simulations support our prediction. In all deep-scenario simulations, where β is negative near the equator, a prograde jet forms at the equator; conversely, in all shallow-scenario simulations, where β is positive close to the equator, a retrograde jet forms at the equator (Fig. 3 and Fig. S1). To test whether there are multiple equilibrium states that favor both prograde and retrograde equatorial jets, we repeated two deep simulations with retrograde equatorial jet in the initial condition, and repeated two shallow simulations with prograde equatorial jet in the initial condition. All experiments end up reversing their equatorial jets (Fig. S2).

PV homogenization occurs in our numerical simulations, where the jet-induced PV compensates for the background planetary PV, forming staircases (Fig. 4a-d and Fig. S3). However, it is worth noting that this compensation is often incomplete, particularly in low-energy deep cases outside the tangent cylinder. This incomplete compensation is likely due to not having enough energy to fully homogenize PV in this

region. To quantify this, we define $\mathcal{R}_{mix} = U_{sim}/U_{mix}$ as the ratio of the diagnosed velocity contrast U_{sim} outside the tangent cylinder to the velocity contrast U_{mix} required for complete PV homogenization (Fig. 4e). If $\mathcal{R}_{mix} \geq 1$, the system has sufficient energy to homogenize PV and vice versa. In most simulations, $\mathcal{R}_{mix} < 1$, indicating incomplete PV homogenization at the equator, consistent with simulation results. In high-energy injection cases where $\mathcal{R}_{mix} > 1$, the available energy is sufficient for PV homogenization outside the tangent cylinder, allowing the jet-induced PV to flatten the PV profile or even overcompensate the planetary PV gradient in simulations (Fig. S3). In addition to the energy limitation, large spatial variations in planetary β make it challenging for the entire domain to satisfy the zonal criterion (37). Despite these limitations, the correlation between equatorial jet direction and the sign of the equatorial β remains robust.

Our results suggest that the direction of the equatorial jet is closely related to the geometry of the system, determined by the penetration depth of the jet D . As D varies, both prograde and retrograde equatorial jets can be reproduced. This mechanism is fundamentally different from pioneer explanations proposed by (15, 25, 26), where the jet direction is connected with the excitation of some dynamic mode, whether it is the Busse mode or the equatorial Rossby mode. The geometric mechanism proposed here and the previous mode-related mechanisms are not mutually exclusive and can superimpose on one another. For example, (25, 26) assumed a shallow geometry for all four giant planets, and found that the equatorial jet is always in retrograde direction unless it is reversed by the convection-excited equatorial Rossby waves. Phenomena-wise, our shallow cases also tend to form retrograde jet at the equator, but it does not reverse

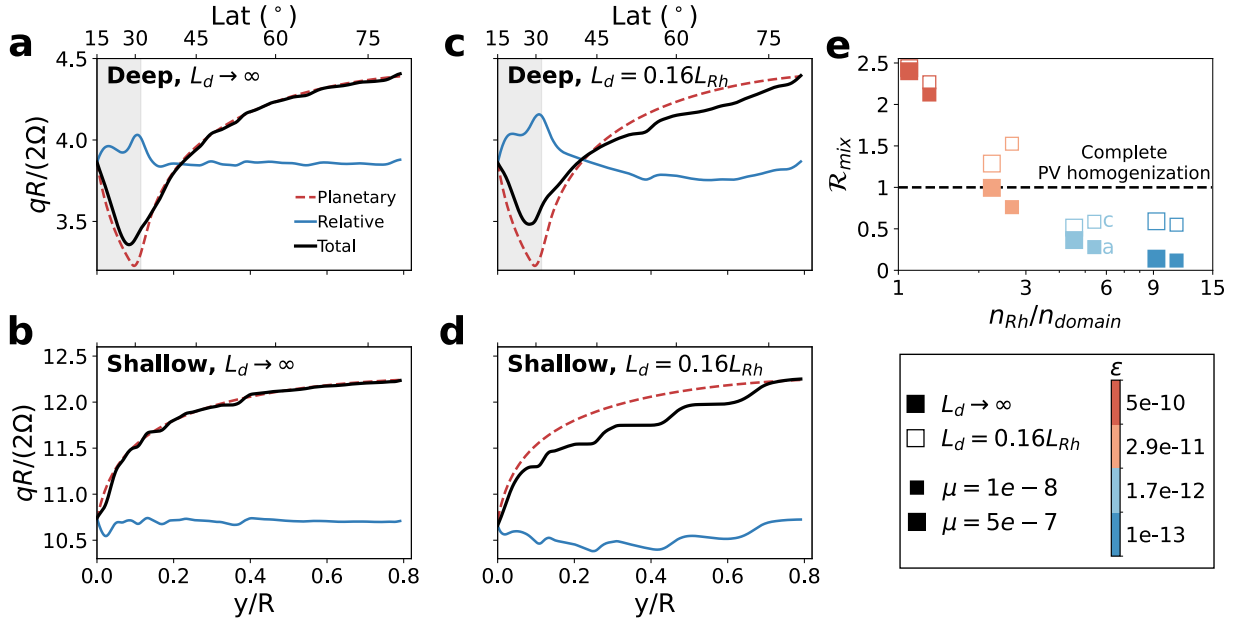


Fig. 4. PV homogenization and staircases. **a-d**, non-dimensionalized zonal-mean PV profile ($qR/(2\Omega)$) in the northern hemisphere, where red line denotes planetary PV ($\overline{q_p} = \int \beta dy = -2\Omega \ln H$), blue line denotes jet-induced relative PV ($\overline{q_r} = -\partial \overline{u}/\partial y - \overline{\psi}/L_d^2$), and black line denotes total PV ($\overline{q} = \overline{q_p} + \overline{q_r}$), where overline denotes zonal average. Simulation results for $\epsilon = 1.7 \times 10^{-12}$ and $\mu = 10^{-7}$ are shown in **a-d**, and results for other simulations are shown in Fig. S3. **e**, the ratio of the diagnosed velocity contrast outside the tangent cylinder to the required velocity contrast to smooth the PV profile outside the tangent cylinder ($\mathcal{R}_{mix} = U_{sim}/U_{mix}$) as a function of the Rhines wavenumber n_{Rh} to the domain wavenumber n_{domain} . U_{sim} is the diagnosed velocity contrast outside the tangent cylinder in the simulations. U_{mix} is the required velocity contrast for complete PV homogenization outside the tangent cylinder, obtained by integrating $\beta - \partial^2 \overline{u}/\partial y^2 + \overline{u}/L_d^2 = 0$ outside the tangent cylinder using β profile in the deep case (Fig. 2b). The black dashed line indicates $\mathcal{R}_{mix} = 1$, i.e. PV homogenization can be completed given the energy provided in the simulation. The simulations shown in **a** and **c** are also marked in **e**.

even in presence of convective forcing, probably due to the lack of equatorial Rossby waves. As another example, (15) assumed a deep geometry and found that equatorial jet is in prograde direction as the thermal Rossby waves pump prograde momentum toward the surface, unless the superfast flow breaks the constraints of planetary rotation ($Ro > 1$). The Rossby numbers $Ro = U/(2\Omega R)$ for all four planets are far smaller than unity as can be seen in Fig. 1, suggesting that some other mechanisms may be needed to explain the retrograde jets on Uranus and Neptune. We think the answer could have already been provided by the shallow geometry mechanism (25, 26), as validated by our shallow scenario. In our work, both the deep geometry and the shallow geometry are investigated in the same framework, and we found that even with $Ro \ll 1$, retrograde jet can still form as long as the shallow geometry is adopted.

The number and smoothness of jets. The tangent cylinder divides the planetary atmosphere into two distinct regions. On Jupiter and Saturn, while multiple jets can form inside the tangent cylinder, the region outside the tangent cylinder only has one single jet. We believe this occurs because the atmosphere outside the tangent cylinder is not in direct contact with the Ohmic dissipation layer, and therefore cannot be damped as effectively as elsewhere. Without damping, jet energy there can accumulate, accompanied by a growth in jet width, until one single jet fills the entire region.

The jet width inside the tangent cylinder follows the Rhines scale L_{Rh} (30). In an unstratified atmosphere, the Rhines scale is given by $L_{Rh} \sim (U/\beta)^{1/2}$. When

stratification is present, it modifies the Rhines scale to $L_{Rh} \sim (\beta/U - L_d^{-2})^{-1/2}$, where L_d is the deformation radius (42). This modified Rhines scale captures the jet width in our numerical simulations fairly well (Fig. 5a). The number of jets, in turn, scales with the ratio of the domain scale to the Rhines scale (Fig. 5b), consistent with findings from previous studies (43–45). In high-energy experiments (denoted by the reddish color in Fig. 5b), the jet number scaling breaks down as the jet width becomes sufficiently large to feel the constraints of the domain. In shallow scenario simulations, one prograde jet must form together with the equatorial retrograde jet by virtue of momentum conservation, resulting in a total of two jets. In the deep scenario, the tangent cylinder further divides the domain into two regions, leading to the formation of three jets, excluding the equatorial one (Fig. 5b).

In the zonostrophic regime, the kinetic energy of zonal jets peaks at larger scales, while the kinetic energy of eddies is primarily concentrated at smaller scales. The β scale L_β is the scale at which eddies begin to cascade their energy into zonal jets, and the jet energy dissipates at the Rhines scale L_{Rh} (31, 46). When more energy is stored in the jets, they appear smoother; conversely, when eddies hold more energy, the jets look more chaotic (47). In the absence of stratification ($L_d \rightarrow \infty$), by integrating the theoretical energy spectrum from n_{Rh} to n_β and from n_β to infinity (infinitely small length scale), we can determine the energy distribution between jets and eddies. This yields the predicted jet energy fraction (see *Supporting Information* for detailed derivation):

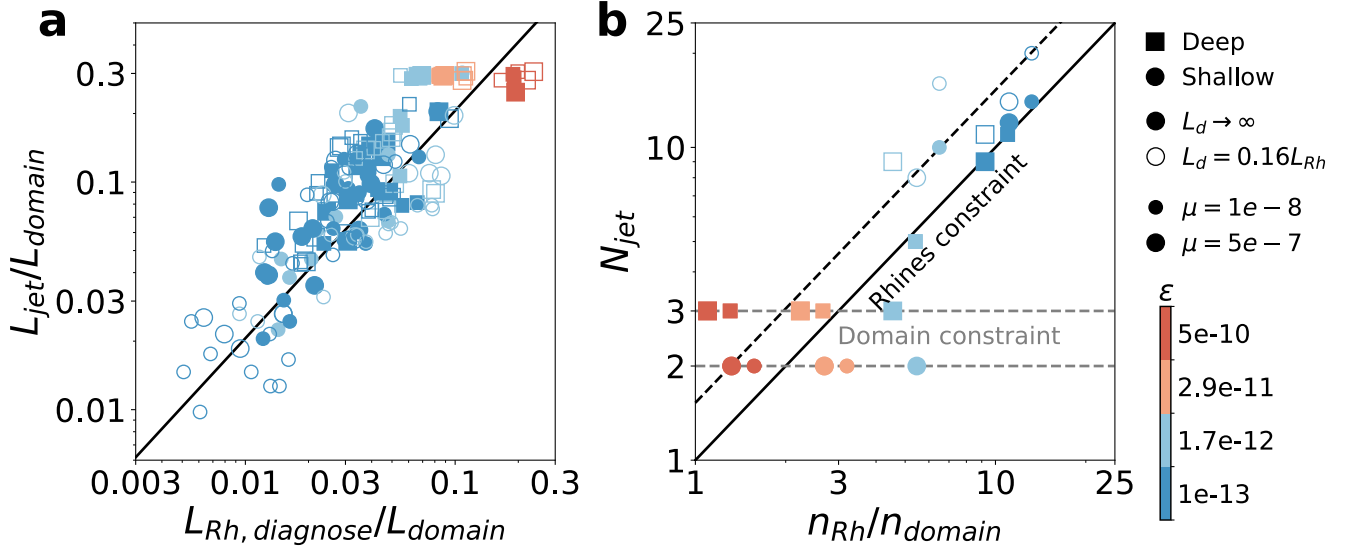


Fig. 5. Jet width and number. **a**, Diagnosed jet width (L_{jet}) compared to the diagnosed modified Rhines scale ($L_{Rh,diagnose}$), both normalized by the domain length scale L_{domain} . **b**, Number of jets (N_{jet}) diagnosed in the simulations compared to the theoretical prediction, n_{Rh}/n_{domain} . Detailed jet diagnostic information is provided in Fig. S1. In **a**, jets with widths of $1/2$ the domain size in the shallow scenario and $1/3$ the domain size in the deep scenario are excluded, as their widths are constrained by the domain size and are not expected to follow Rhines scaling. The black solid line represents a fitted line. In **b**, the black solid line is the one-to-one line, and the black dashed line indicates the adjusted prediction, incorporating the fitted factor of jet width to Rhines scale from **a**. Gray dashed lines represent predictions where the jet scale is constrained by the domain size: $N_{jet} = 3$ for the deep scenario and $N_{jet} = 2$ for the shallow scenario. In **a** and **b**, regions outside the tangent cylinder in the deep scenario are excluded.

$$\frac{E_{jet}}{E_{tot}} = \frac{(n_{\beta}/n_{Rh})^4 - 1}{(n_{\beta}/n_{Rh})^4 + 5 - 4(n_{\beta}/n_e)^{2/3}}. \quad [3]$$

This estimate reasonably well predicts the outcomes observed in numerical simulations (Fig. S4). Equation 3 shows that E_{jet}/E_{tot} is primarily influenced by n_{β}/n_{Rh} , assuming that n_e is significantly larger than n_{β} (Table 1). A greater separation between n_{β} and n_{Rh} leads to more energy being stored in jets rather than eddies, making this ratio a useful qualitative metric for predicting the jet energy fraction. By substituting the definitions of n_{β} and n_{Rh} , we find that $n_{\beta}/n_{Rh} \sim \varepsilon^{1/20} \beta^{1/10} \mu^{-1/4}$. Consequently, higher energy injection rate ε , higher β value (indicating either faster rotation rate or smaller planetary radius), or weaker large-scale damping μ , results in more energy concentrated in the jets, making them smoother.

Discussion

We use a stochastically forced 2-D quasi-geostrophic framework to investigate the factors controlling the direction of the equatorial jet and the number of jets in each hemisphere. First, we find that the equatorial jet's direction is primarily set by the sign of the equatorial planetary potential vorticity (PV) gradient, which depends on the jet's penetration depth. Second, we find that the number of jets is well predicted by the ratio of the domain scale (planetary radius for an entire hemisphere) to the Rhines scale, which can be estimated from the observable characteristic flow speed.

When the jet penetration depth is deep, a prograde jet forms at the equator to compensate the negative PV gradient outside the tangent cylinder. When the jet penetration depth is shallow, a retrograde jet forms as the equatorial PV gradient becomes positive. For Jupiter and Saturn, the estimated jet

penetration depths are approximately 3000 km (40, 48) and 8000 km (41), respectively, which implies that the planetary β is negative within 15°N/S and 31°N/S on these two planets. PV homogenization within these latitudinal bands would favor a prograde equatorial jet, consistent with observations. This equatorial jet outside the tangent cylinder is also stronger than the higher-latitude jets due to the lack of damping (Fig. 3b), also consistent with observations (Fig. 1a). For Uranus and Neptune, the jet penetration depths are less well constrained (38). However, their observed retrograde equatorial jets appear incompatible with a deep geometry and low Rossby number (15), instead aligning more closely with a shallow geometry scenario, suggesting the presence of a stratified layer or Ohmic dissipation layer near their surfaces (49–51). In a shallow system, the positive-definite β would drive a retrograde equatorial jet through PV homogenization. Also, the absence of a region outside the tangent cylinder would prevent the shallow system from forming an excessively strong equatorial jet relative to the high-latitude jets (Fig. 3c). Both features are consistent with observations (Fig. 1b).

Beyond the equatorial jet direction, our theory also provides predictions on the number of mid-latitude jets. In the zonostrophic regime, jet width is controlled by the Rhines scale, and the ratio of the domain scale to the Rhines scale determines the number of jets within the tangent cylinder. When the Rhines scale is comparable to the domain size, only one single wide jet forms at mid- and high-latitudes. On Jupiter and Saturn, multiple alternating jets are observed at mid-latitudes, consistent with our theoretical predictions. On Uranus and Neptune, there is only one prominent prograde jet in each hemisphere outside the equatorial region, which also aligns with our theoretical prediction (Fig. 3 & Fig. 5b). The mechanism that sustains such strong jets on Uranus and Neptune remains unclear and requires further investigation.

It should be noted that our model is highly idealized, designed to represent two jet formation mechanisms within a unified framework, allowing us to focus on the inverse energy cascade process shared by both. To this end, some aspects of the physics involved in eddy generation are neglected, where energy is introduced as stochastic noise. However, the simplified processes may still contribute to momentum transport and influence jet structure. These effects can be superimposed onto our framework to provide a more comprehensive understanding of jet dynamics on giant planets. For example, interior heating in a deep atmosphere can generate thermal Rossby waves at the equator, known as the Busse mode (9). This mode has a spatially tilted structure, which preferentially transports prograde momentum toward the equatorial surface, resulting in a prograde equatorial jet (15). Additionally, solar forcing induces stratification in the upper atmosphere, storing potential energy. In a stratified atmosphere, the meridional temperature gradient from differential solar heating at different latitudes drives baroclinic instabilities. Baroclinic instabilities arise when the PV gradient changes sign, which can happen at mid-latitudes where strong thermal wind shear exists (26), or outside the tangent cylinder where β changes sign due to the spherical geometry (52). These instabilities convert potential energy into eddy kinetic energy, thereby converging momentum and leading to the formation of jets where the instability occurs (29). Waves originating from lower layers may propagate upwards, get dissipated and transport momentum there, and induce long-term variations in jet speed (53–55).

Despite these potential complexities, our work demonstrates that jet penetration depth can strongly influence surface wind patterns, suggesting that the interior structures of giant planets might be inferred solely from surface features. These projections can be validated through improved characterization of the gravity field by future missions.

Data Archival. The numerical simulations are based on [Dedalus](#). Our code is available on [Github](#).

ACKNOWLEDGMENTS. We thank Keaton Burns and Daniel Lecoanet for their assistance in setting up the Dedalus numerical model. We thank Yohai Kaspi, Philip Marcus, Jiaru Shi, and Huazhi Ge for helpful discussions. This work originates during the 2023 Geophysical Fluid Dynamics (GFD) Summer School at Woods Hole. We thank the GFD faculty for organizing the program and the Woods Hole Oceanographic Institution for hosting it. The numerical simulations were performed using the svante cluster in the Department of Earth, Atmospheric, and Planetary Sciences (EAPS) at MIT. We thank Jeffery Scott and Morgan Ludwig for their technical support. For the purpose of open access the authors have applied a Creative Commons Attribution (CC BY) licence to any Author Accepted Manuscript version arising from this submission.

1. SS Limaye, Jupiter: New estimates of the mean zonal flow at the cloud level. *Icarus* **65**, 335–352 (1986).
2. LA Sromovsky, SS Limaye, PM Fry, Dynamics of neptune’s major cloud features. *Icarus* **105**, 110–141 (1993).
3. A Sanchez-Lavega, JF Rojas, PV Sada, Saturn’s zonal winds at cloud level. *Icarus* **147**, 405–420 (2000).
4. E Garcia-Melendo, A Sánchez-Lavega, A study of the stability of jovian zonal winds from hst images: 1995–2000. *Icarus* **152**, 316–330 (2001).
5. E Garcia-Melendo, S Pérez-Hoyos, A Sánchez-Lavega, R Hueso, Saturn’s zonal wind profile in 2004–2009 from cassini iss images and its long-term variability. *Icarus* **215**, 62–74 (2011).
6. L Sromovsky, I de Pater, P Fry, H Hammel, P Marcus, High s/n keck and gemini ao imaging of uranus during 2012–2014: new cloud patterns, increasing activity, and improved wind measurements. *Icarus* **258**, 192–223 (2015).

7. J Tollefson, et al., Changes in jupiter’s zonal wind profile preceding and during the juno mission. *Icarus* **296**, 163–178 (2017).
8. A Sánchez-Lavega, et al., Zonal jets in gas giants. *Zonal jets* pp. 9–45 (2019).
9. FH Busse, Thermal instabilities in rapidly rotating systems. *J. Fluid Mech.* **44**, 441–460 (1970).
10. FH Busse, A simple model of convection in the jovian atmosphere. *Icarus* **29**, 255–260 (1976).
11. UR Christensen, Zonal flow driven by deep convection in the major planets. *Geophys. research letters* **28**, 2553–2556 (2001).
12. UR Christensen, Zonal flow driven by strongly supercritical convection in rotating spherical shells. *J. Fluid Mech.* **470**, 115–133 (2002).
13. M Heimpel, J Aurnou, J Wicht, Simulation of equatorial and high-latitude jets on jupiter in a deep convection model. *Nature* **438**, 193–196 (2005).
14. M Heimpel, J Aurnou, Turbulent convection in rapidly rotating spherical shells: A model for equatorial and high latitude jets on jupiter and saturn. *Icarus* **187**, 540–557 (2007).
15. J Aurnou, M Heimpel, J Wicht, The effects of vigorous mixing in a convective model of zonal flow on the ice giants. *Icarus* **190**, 110–126 (2007).
16. Y Kaspi, GR Flierl, AP Showman, The deep wind structure of the giant planets: Results from an anelastic general circulation model. *Icarus* **202**, 525–542 (2009).
17. CA Jones, KM Kuzanyan, Compressible convection in the deep atmospheres of giant planets. *Icarus* **204**, 227–238 (2009).
18. K Soderlund, M Heimpel, E King, J Aurnou, Turbulent models of ice giant internal dynamics: Dynam. heat transfer, and zonal flows. *Icarus* **224**, 97–113 (2013).
19. T Gastine, J Wicht, J Aurnou, Zonal flow regimes in rotating anelastic spherical shells: An application to giant planets. *Icarus* **225**, 156–172 (2013).
20. T Gastine, M Heimpel, J Wicht, Zonal flow scaling in rapidly-rotating compressible convection. *Phys. Earth Planet. Interiors* **232**, 36–50 (2014).
21. GP Williams, Planetary circulations: 1. barotropic representation of jovian and terrestrial turbulence. *J. Atmospheric Sci.* **35**, 1399–1426 (1978).
22. JY Cho, LM Polvani, The morphogenesis of bands and zonal winds in the atmospheres on the giant outer planets. *Science* **273**, 335–337 (1996).
23. AP Showman, Numerical simulations of forced shallow-water turbulence: Effects of moist convection on the large-scale circulation of jupiter and saturn. *J. Atmospheric Sci.* **64**, 3132–3157 (2007).
24. R Scott, LM Polvani, Equatorial superrotation in shallow atmospheres. *Geophys. Res. Lett.* **35** (2008).
25. T Schneider, J Liu, Formation of jets and equatorial superrotation on jupiter. *J. Atmospheric Sci.* **66**, 579–601 (2009).
26. J Liu, T Schneider, Mechanisms of jet formation on the giant planets. *J. Atmospheric Sci.* **67**, 3652–3672 (2010).
27. Y Lian, AP Showman, Generation of equatorial jets by large-scale latent heating on the giant planets. *Icarus* **207**, 373–393 (2010).
28. Y Kaspi, *Turbulent convection in an anelastic rotating sphere: A model for the circulation on the giant planets.* (Massachusetts Institute of Technology), (2008).
29. GK Vallis, *Essentials of atmospheric and oceanic dynamics.* (Cambridge university press), (2019).
30. PB Rhines, Waves and turbulence on a beta-plane. *J. Fluid Mech.* **69**, 417–443 (1975).
31. GK Vallis, ME Maltrud, Generation of mean flows and jets on a beta plane and over topography. *J. physical oceanography* **23**, 1346–1362 (1993).
32. P Marcus, A numerical simulation of the great red spot of jupiter. *Nature* **331**, 693–696 (1988).
33. PS Marcus, Prediction of a global climate change on jupiter. *Nature* **428**, 828–831 (2004).
34. J Liu, PM Goldreich, DJ Stevenson, Constraints on deep-seated zonal winds inside jupiter and saturn. *Icarus* **196**, 653–664 (2008).
35. M French, et al., Ab initio simulations for material properties along the jupiter adiabat. *The Astrophys. J. Suppl. Ser.* **202**, 5 (2012).
36. D Soyuer, F Soubiran, R Helled, Constraining the depth of the winds on uranus and neptune via ohmic dissipation. *Mon. Notices Royal Astron. Soc.* **498**, 621–638 (2020).
37. B Galperin, S Sukoriansky, N Dikovskaya, Zonostrophic turbulence. *Phys. Scripta* **2008**, 014034 (2008).
38. Y Kaspi, AP Showman, WB Hubbard, O Aharanson, R Helled, Atmospheric confinement of jet streams on uranus and neptune. *Nature* **497**, 344–347 (2013).
39. A Sánchez-Lavega, M Heimpel, Atmospheric dynamics of giants and icy planets. *Handb. exoplanets* p. 51 (2018).
40. Ye Kaspi, et al., Jupiter’s atmospheric jet streams extend thousands of kilometres deep. *Nature* **555**, 223–226 (2018).
41. E Galanti, et al., Saturn’s deep atmospheric flows revealed by the cassini grand finale gravity measurements. *Geophys. Res. Lett.* **46**, 616–624 (2019).
42. J Theiss, A generalized rhines effect and storms on jupiter. *Geophys. research letters* **33** (2006).
43. S Sukoriansky, N Dikovskaya, B Galperin, On the arrest of inverse energy cascade and the rhines scale. *J. Atmospheric Sci.* **64**, 3312–3327 (2007).
44. TJ Dunkerton, RK Scott, A barotropic model of the angular momentum-conserving potential vorticity staircase in spherical geometry. *J. Atmospheric Sci.* **65**, 1105–1136 (2008).
45. D Lemasquerier, B Favier, M Le Bars, Zonal jets experiments in the gas giants’ zonostrophic regime. *Icarus* **390**, 115292 (2023).
46. M Maltrud, G Vallis, Energy spectra and coherent structures in forced two-dimensional and beta-plane turbulence. *J. Fluid Mech.* **228**, 321–342 (1991).
47. RK Scott, DG Dritschel, The structure of zonal jets in geostrophic turbulence. *J. Fluid Mech.* **711**, 576–598 (2012).
48. H Cao, et al., Strong resemblance between surface and deep zonal winds inside jupiter revealed by high-degree gravity moments. *The Astrophys. J.* **959**, 78 (2023).
49. PN Wulff, W Dietrich, UR Christensen, J Wicht, Zonal winds in the gas planets driven by convection above a stably stratified layer. *Mon. Notices Royal Astron. Soc.* **517**, 5584–5593

(2022).

50. P Wulff, UR Christensen, W Dietrich, J Wicht, The effects of a stably stratified region with radially varying electrical conductivity on the formation of zonal winds on gas planets. *J. Geophys. Res. Planets* **129**, e2023JE008042 (2024).
51. UR Christensen, PN Wulff, Quenching of zonal winds in jupiter's interior. *Proc. Natl. Acad. Sci.* **121**, e2402859121 (2024).
52. Y Kaspi, GR Flierl, Formation of jets by baroclinic instability on gas planet atmospheres. *J. Atmospheric Sci.* **64**, 3177–3194 (2007).
53. CB Leovy, AJ Friedson, GS Orton, The quasiquadrennial oscillation of jupiter's equatorial stratosphere. *Nature* **354**, 380–382 (1991).
54. T Fouchet, et al., An equatorial oscillation in saturn's middle atmosphere. *Nature* **453**, 200–202 (2008).
55. AP Showman, X Tan, X Zhang, Atmospheric circulation of brown dwarfs and jupiter-and saturn-like planets: zonal jets, long-term variability, and qbo-type oscillations. *The Astrophys. J.* **883**, 4 (2019).